



WRF-Chem v3.9 simulations of the East Asian dust storm in May 2017: modeling sensitivities to dust emission and dry deposition schemes

Yi Zeng^{1,2}, Minghuai Wang^{1,2}, Chun Zhao³, Siyu Chen⁴, Zhoukun Liu^{1,2}, Xin Huang^{1,2}, Yang Gao⁵

¹Institute for Climate and Global Change Research and School of Atmospheric Sciences, Nanjing University, 210023
5 Nanjing, China

²Joint International Research Laboratory of Atmospheric and Earth System Sciences & Institute for Climate and Global
Change Research, Nanjing University, China

³School of Earth and Space Sciences, University of Science and Technology of China, Hefei, 230026, China

⁴Key Laboratory for Semi-Arid Climate Change of the Ministry of Education, College of Atmospheric Sciences, Lanzhou
10 University, Lanzhou, 730000, China

⁵Key Laboratory of Marine Environment and Ecology, Ministry of Education/Institute for Advanced Ocean Study,
Ocean University of China, and Qingdao National Laboratory for Marine Science and Technology, Qingdao, 266100,
China

Correspondence to: Minghuai Wang (minghuai.wang@nju.edu.cn)

15 **Abstract**

Dust aerosol plays an important role in the radiative budget and hydrological cycle, but large uncertainties remain for
simulating dust emission and dry deposition processes in models. In this study, we investigated dust simulation sensitivity to
two dust emission schemes and three dry deposition schemes using Weather Research and Forecasting model coupled with
chemistry (WRF-Chem). Results showed that simulated dust loading is very sensitive to different dry deposition schemes,
20 with the relative difference of dust loading using different dry deposition schemes range from 20%-116%. Two dust
emission schemes are found to produce significantly different spatial distribution of dust loading. The difference of dry
deposition velocity in different dry deposition schemes comes from the parameterization of collection efficiency from
impaction and rebound effect. An optimal combination of dry deposition scheme and dust emission scheme has been
identified to best simulate the dust storm in comparison with observation and to include better physical treatment of dust



25 emission and surface collection processes. The optimal dry deposition scheme accounts for the rebound effect and the collection efficiency from impaction changes with the land use categories and therefore has a better physical treatment of dry deposition velocity. Our results highlight the importance of dry deposition schemes for dust simulation.

1 Introduction

Dust aerosol is an important component in the atmosphere and it can impact many processes of the Earth system. Through absorbing and scattering shortwave and longwave radiative fluxes, dust can alter the radiative budgets, which is called the direct effect (Chen et al., 2013; Kok et al., 2017; Zhao et al., 2010, 2011, 2012). Acting as cloud condensation nuclei (CCN) and ice nuclei (IN), dust can change cloud properties and precipitation, which is called the indirect effects (Creamean et al., 2013; Demott et al., 2010). Besides, dust aerosol can absorb solar radiation and change the atmospheric stability and therefore cloud formation, which is known as the semi-direct effect (Hansen et al., 1997). Furthermore, natural dust is important for air quality assessments and has significant impacts on human health (Abuduwaili et al., 2010; Chen et al., 2019; Hofer et al., 2017; Jiménez-Guerrero et al., 2008; Ozer et al., 2007). Although great progress has been made in dust models and dust simulations in recent decades, large uncertainties remain in dust simulations (Huneeus et al., 2011; Prospero et al., 2010; Todd et al., 2008; Uno et al., 2006; Zender et al., 2004; Zhao et al., 2013).

A complete description of dust events includes dust emission, deposition and transport processes. The differences of dust simulation mainly result from the uncertainties of dust emission, deposition and transport processes in models. One uncertainty is from dry deposition processes. Dry deposition refers to the transport of particles from the atmosphere to the Earth's surface in the absence of precipitation (Seinfeld and Pandis, 2006). In most aerosol modeling, dry deposition velocity V_d is used to calculate the dry deposition flux and V_d is usually modelled using the resistance-based approach (Pryor et al., 2008). In the resistance-based approach, V_d is determined by gravitational settling, aerodynamic resistance and surface resistance. Surface resistance is determined by collection efficiency from Brownian diffusion, impaction and interception and is corrected for particle rebound. Slinn (1982) proposed a semi-analytical description of particle collection efficiencies based on the wind tunnel studies, and many dry deposition schemes since then are variants of this model (Binkowski and Shankar, 1995; Giorgi, 1986; Peters and Eiden, 1992; Zhang et al., 2001). As the formulations for collection efficiencies



from different dry deposition schemes are derived from measurements that have been obtained under different meteorological conditions and land surface types, there remains a large discrepancy of these formulations between different dry deposition models (Petroff et al., 2008).

At present, the comparisons of different dry deposition schemes with reliable field measurements are mainly focused on one-dimensional dry deposition models (Hicks et al., 2016; Khan and Perlinger, 2017; Petroff et al., 2008; Ruijrok et al., 1995). For example, Hicks et al. (2016) compared five deposition models with observations and found that V_d predicted for particles less than $0.2 \mu\text{m}$ is consistent with the measurements, but predicted V_d can vary greatly in the size range of 0.3 to about $5 \mu\text{m}$. However, few studies have been conducted to study how different dry deposition schemes affect aerosol concentrations and their spatial distribution in the 3D numerical models. Wu et al. (2018) compared the effects of different dry deposition schemes on black carbon simulation in a global climate model (CESM-CAM5), but did not examine how different dry deposition schemes affect aerosol concentrations for large-size aerosol particles, such as dust.

Another uncertainty of dust simulation is the treatment of dust emission process in models. Natural dust is typically emitted from dry, erodible surfaces when the wind speed is high. Dust emission process is closely related to soil texture, soil moisture content, surface conditions, atmospheric stability and the wind velocity (Marticorena and Bergametti, 1995). Dust emission schemes are used to predict the dust emission flux and to describe the dust size distribution. Many studies have compared and evaluated the performance of different dust emission schemes (Kang et al., 2011; LeGrand et al., 2019; Su and Fung, 2015; Wu and Lin, 2013, 2014; Yuan et al., 2019; Zhao et al., 2010, 2006). These studies show large diversity of simulated dust emission flux among different dust emission schemes. Zhao et al. (2006) implemented two dust emission schemes in the NARCM (Northern Aerosol Regional Climate Model) regional model, and found that both schemes captured the dust mobilization episodes and produced the similar spatial distributions of dust loading over East Asia, but the dust emission fluxes and surface concentrations differ a lot. Kang et al. (2011) compared three dust emission schemes in WRF-Chem and found that the difference between the vertical dust fluxes derived from the three emission schemes can reach to several orders of magnitude. Yuan et al. (2019) found that one scheme strongly underestimated the dust emission while another two schemes can better show the spatial and temporal variation of dust AOD based on a storm outbreak in Central Asia. These differences mainly come from the dust emission flux parameterizations and differences in soil and



surface input parameters in different dust emission schemes (Chen et al., 2017).

75 While dust emission schemes have been studied quite extensively, few studies have examined dust emission and dry deposition schemes simultaneously. As both dust emission schemes and dry deposition schemes contribute significantly to the uncertainties in dust simulations, evaluating dust schemes based on a single dry deposition scheme may be problematic, especially if the dry deposition schemes employed have deficiency. For example, as a widely used regional model that has been coupled with a variety of dust emission schemes, the WRF-Chem model has been used in many studies to evaluate the performance of dust emission schemes (LeGrand et al., 2019; Su and Fung, 2015; Wu and Lin, 2013, 2014; Yuan et al., 80 2019). But most of these studies use the GOCART aerosol scheme and only one dry deposition scheme (Wesely, 1989) is coupled within the GOCART aerosol scheme. Zhang et al. (2019) compared the modelled dust deposition using the GOCART aerosol scheme in WRF-Chem with observed dust deposition, and found that modelled dust deposition is highly underestimated by more than one order of magnitude compared to the observed deposition. This indicates that the dry 85 deposition scheme (Wesely, 1989) in GOCART aerosol scheme may not be suitable for dust simulation and needs to be further improved.

In this study, we adopted the MOSAIC aerosol scheme coupled within the WRF-Chem model to study how dry deposition schemes and dust emission schemes affect dust simulations by evaluating model results against observations. As the MOSAIC aerosol scheme includes several different dry deposition schemes, this allows us to choose more advanced dry 90 deposition schemes. As the default MOSAIC aerosol scheme only includes the GOCART dust emission scheme, we further implemented the dust emission scheme Shao2011 (Shao et al., 2011) in the MOSAIC aerosol scheme, which allows us to compare these two widely used dust schemes along with multiple dry deposition schemes. The goals of this study are: (1) to study dust simulation sensitivity to different dust emission schemes and dry deposition schemes, (2) to explore which combination of dust emission scheme and dry deposition scheme can better simulate dust storms in East Asia. The paper is 95 organized as follows. Sect. 2 introduces the WRF-Chem model, dust emission schemes and dry deposition schemes used, experiments design and measurements. Sect. 3 analyzes the dust simulation sensitivity to dust emission schemes and dry deposition schemes and the comparisons with observations. Sect. 4 is the summary and discussion.



2 Methodology and measurements

2.1 Model description

100 In this study, WRF-Chem version 3.9 is used. WRF-Chem is built based on the regional mesoscale model WRF, and fully coupled with gas and aerosol chemistry module (Grell et al., 2005). The model setups are listed in Table 1. The Noah land surface model (Chen and Dudhia, 2001) and the Yonsei University (YSU) planetary boundary scheme (Hong et al., 2006) are used in this study. The Rapid Radiative Transfer Model for General Circulation (RRTMG) radiation scheme (Iacono et al., 2008) is used to calculate the longwave and shortwave radiation. The Grell-Freitas convective scheme (Grell and Freitas, 2014) and the Morrison two-moment microphysics scheme (Morrison et al., 2008) are used. The gas-phase chemistry module used is the Carbon-Bond Mechanism version Z (CBMZ, Zaveri and Peters, 1999). The aerosol module used here is the Model for Simulating Aerosol Interactions and Chemistry with 4 bins (MOSAIC 4-bin) (Zaveri et al., 2008). The MOSAIC aerosol scheme uses sectional approach to represent aerosol size distribution. The MOSAIC 4-bin aerosol scheme divides aerosol particles into four size bins by aerosol diameter: 0.039-0.156, 0.156-0.625, 0.625-2.5, 2.5-10.0 μm . The MOSAIC aerosol scheme includes sulfate, methane sulfonate, nitrate, chloride, carbonate, ammonium, sodium, calcium, black carbon (BC), primary organic mass (OC), liquid water and other inorganic mass (OIN). The OIN species include silica, other inert minerals and trace metals. The emitted dust from dust emission schemes is assigned to the OIN class of MOSAIC to simulate the major aerosol processes. To study the sensitivity of dust simulation to different dust emission schemes and dry deposition schemes, we test two different dust emission schemes (see Sect. 2.2) and three dry deposition schemes (see Sect. 2.3) within MOSAIC.

115

2.2 Dust emission schemes

Dust emission schemes include empirical schemes and schemes based on dust physical processes. Because of differences in input parameters and formulas to calculate dust flux, dust emission varies among different dust emission schemes. The Goddard Chemistry Aerosol Radiation and Transport (GOCART) dust emission scheme (Ginoux et al., 2001) is an empirical scheme and was implemented in MOSAIC by Zhao et al. (2010). The University of Cologne (UoC) dust emission schemes

120



(Shao, 2001, 2004; Shao et al., 2011) (Shao schemes) are size-resolved dust emission scheme based on the wind erosion physical theory. Shao2011 (Shao et al., 2011) is a simplified version of Shao2004 (Shao, 2004), but the performances of the full scheme (Shao2004) and the simplified scheme are equally effective (Shao et al., 2011). The Shao dust emission schemes are widely used for dust simulations in East Asia, and have been found to perform well in simulating dust emission fluxes (Shao et al., 2011; Su and Fung, 2015; Wu and Lin, 2014). Therefore, to test the sensitivity of dust simulation to different dust emission schemes, we implemented the Shao2011 dust emission scheme in MOSAIC. Each dust emission scheme is described in detail below.

2.2.1 GOCART

The formula of vertical dust flux in GOCART is approximated as:

$$130 \quad F_p = \begin{cases} CSs_p u_{10}^2 (u_{10} - u_t) & \text{if } u_{10} > u_t \\ 0 & \text{otherwise} \end{cases} \quad (1)$$

where C is an empirical proportionality constant and S is the source function. s_p is the fraction of each size class of the emitted dust. u_{10} is the horizontal wind speed at 10 meters. u_t is the threshold wind speed below which the dust emission does not occur. The emitted dust emission flux from GOCART scheme is re-distributed into different bins for MOSAIC as Zhao et al. (2010).

135 2.2.2 Shao2011

The Shao2011 dust emission scheme is a size-resolved dust emission scheme based on the wind erosion physical theory. The dust flux is determined by:

$$140 \quad F(d_i, d_s) = c_y \eta_{mi} (1 + \sigma_m) g \frac{Q(d_s)}{u^2} \quad (2)$$

where $F(d_i, d_s)$ is the dust emission rate of particle size d_i generated by the saltation of particles of sizes d_s ; c_y is the dimensionless coefficient; η_{mi} is the mass fraction of free dust for a unit soil mass; σ_m is bombardment efficiency; $Q(d_s)$ is the saltation flux averaged over the range of sand particle sizes. As the Shao2011 scheme is a size-resolved dust emission scheme, we cut the size bins for MOSAIC aerosol scheme from Shao2011 directly. The details of the Shao2011 dust emission



scheme are described in Appendix A. There is a bug in calculating dust emission flux in Shao2011 scheme reported after WRF-Chem v3.9, we have already corrected it in our simulation (See Appendix A). We should mention that the Shao2011 dust emission scheme used in this study is not the original version in WRF-Chem v3.9 and the details will be discussed in Sect. 3.1 and Appendix B.

2.3 Dry deposition schemes

For dry deposition schemes, dry deposition velocity (V_d) is used to calculate dry deposition flux. V_d is determined by gravitational settling velocity (V_g), aerodynamic resistance (R_a) and surface resistance (R_s). There are three dry deposition schemes available in WRF-Chem coupled with the MOSAIC module and used in this study as referred to BS95 (Binkowski and Shankar, 1995), PE92 (Peters and Eiden, 1992) and Z01 (Zhang et al., 2001). Each dry deposition scheme will be described in detail below.

2.3.1 BS95

In the BS95 scheme (Binkowski and Shankar, 1995), V_d is expressed as:

$$V_d = V_g + \frac{1}{R_a + R_s + R_a R_s V_g} \quad (3)$$

where R_a and R_s are aerodynamic and surface resistance; V_g is the gravitational settling velocity and is given as:

$$V_g = \frac{\rho_p d_p^2 g C_c}{18\mu} \quad (4)$$

where ρ_p is the density of particles, d_p is particle diameter, C_c is the Cunningham correction factor as a function of d_p and mean free path of air (λ), and μ is the viscosity dynamic of air. The surface resistance is calculated as:

$$R_s = \frac{1}{u_* (E_B + E_{IM})} \quad (5)$$

where E_B and E_{IM} are collection efficiencies from Brownian diffusion and impaction, respectively. E_B and E_{IM} are calculated as follows:

$$E_B = Sc^{-\frac{2}{3}} \quad (6)$$



$$E_{IM} = 10^{-\frac{3}{St}} \quad (7)$$

165 where Sc is the Schmidt number, given by $Sc = \nu/D$. ν is the kinematic viscosity of air and D is the particle Brownian diffusivity. St is the Stokes number, given by:

$$St = \frac{u_z^2 v_g}{g\nu} \quad (8)$$

2.3.2 PE92

In PE92 scheme (Peters and Eiden, 1992), the dry deposition velocity (V_d) is expressed as:

$$170 \quad V_d = V_g + \frac{1}{R_a + R_s} \quad (9)$$

The formula of V_g and R_a is the same as in BS95, but the way to calculate R_s is quite different. In PE 92, R_s is parametrized as:

$$R_s = \frac{1}{u_* (E_B + E_{IM} + E_{IN}) R} \quad (10)$$

175 where E_{IN} is collection efficiency from impaction and R is the factor for particle rebound. E_{IM} , E_{IN} and R are expressed as follows:

$$E_{IM} = \left(\frac{St}{0.8 + St} \right)^2 \quad (11)$$

$$E_{IN} = \frac{(0.0016 + 0.0061z_0)d_p}{1.414 \times 10^{-7}} \quad (12)$$

$$R = e^{-2\sqrt{St}} \quad (13)$$

z_0 is the roughness length and d_p is particle diameter. Stokes number is given by:

$$180 \quad St = \frac{\rho_p d_p^2 u}{9\mu d_c} \quad (14)$$

u is the horizontal wind velocity, d_c is the diameter of the obstacle.

2.3.3 Z01

In Z01 scheme (Zhang et al., 2001), the formula of V_d is the same as in BS95 scheme (Eq. (3)). Surface resistance R_s is



calculated as:

$$185 \quad R_S = \frac{1}{\epsilon_0 u_* (E_B + E_{IM} + E_{IN}) R} \quad (15)$$

$$E_B = S c^{-\gamma} \quad (16)$$

where γ depends on land use categories (LUC) and lies between 1/2 and 2/3.

E_{IM} is expressed as:

$$E_{IM} = \left(\frac{St}{\alpha + St} \right)^\beta \quad (17)$$

190 where β equals to 2 and α depends on LUC. The Stokes number is given by:

$$St = V_g u_* / g A \quad (18)$$

over vegetated surfaces (Slinn, 1982) and

$$St = V_g u_*^2 / g \nu \quad (19)$$

over smooth surfaces or surfaces with bluff roughness elements (Giorgi, 1988). E_{IN} is expressed as:

$$195 \quad E_{IN} = \frac{1}{2} \left(\frac{dp}{A} \right)^2 \quad (20)$$

over vegetated surfaces and $E_{IN} = 0$ for non-vegetated surfaces, where A is the characteristic radius of collectors and depends on LUC. R is expressed as:

$$R = e^{-1.0\sqrt{St}} \quad (21)$$

The main difference of formulas used to calculate dry deposition velocity for three different dry deposition schemes are
 200 listed in Table 2. For surface resistance parameterization, PE92 and Z01 include the rebound effect and collection efficiency from interception, while BS95 neglects the rebound effect and collection efficiency from interception. For the collection efficiency from impaction parameterization, all three schemes use Stokes number to parameterize E_{IM} , but the formulas are quite different. BS95 has a different formula from PE92 and Z01, while the PE92 and Z01 have the same formula but with different coefficients. For PE92, the coefficient for E_{IM} is constant for all the surface types. For Z01, the coefficients α and
 205 β for E_{IM} change with different surface types. For the collection efficiency from interception parameterization, BS95 ignores this effect; PE92 and Z01 use different formulas and variables to calculate E_{IN} . For rebound effect, BS95 does not



consider the rebound effect; PE92 and Z01 use the same e-exponential form $e^{-bv\sqrt{St}}$ to calculate the rebound effect with different coefficient b . For PE92, b is 2.0; for Z01, b is 1.0. In addition, the parameterization of Stokes number is quite different for different dry deposition schemes. For BS95, the formulation of St tends to emphasize the nature of the flow field (Binkowski and Shankar, 1995; Pryor et al., 2008). For Z01, the formulation of St is from Slinn (1982) over vegetated surfaces and from Binkowski and Shankar (1995) over smooth surfaces. The formulation of St from Slinn (1982) and Peters and Eiden (1992) are focus on the individual obstacles (Pryor et al., 2008).

2.4 Experiments Design

We use WRF-Chem v3.9 with $20 \text{ km} \times 20 \text{ km}$ horizontal resolution to simulate the dust storm in May 2017. The domain covers most of the East Asia ($14\text{-}60^\circ\text{N}$, $74\text{-}130^\circ\text{E}$). The simulation period is from 26 April to 7 May 2017. During this period, a severe dust storm event originated from northwestern China and Outer Mongolia, and air quality deteriorated dramatically in a very short time in downwind areas (Guo et al., 2019; Zhang et al., 2018). Meteorological conditions are initialized and forced at the lateral boundaries using the 6-hourly National Center for Environmental Prediction Final (NECP FNL) Operational Global Analysis data at a resolution of $1^\circ \times 1^\circ$. The meteorological conditions are reinitialized every 24 hours. This method has already been used in other simulations (Su and Fung, 2015; Zhang et al., 2016), which has been verified that a better meteorological field can be obtained. The output of the aerosol field from the previous 1-day run was used as the initial chemical conditions for the next 1-day run. The MOSAIC aerosol scheme was used for all the simulations. Simulation results prior to 28 April are treated as model spin up for chemical initial condition and are not included in results presented in Sect. 3. The model results from 1 May to 7 May are used for the dust loading and concentration analysis. And the model results from 28 April to 7 May are used for the dust emission analysis as the dust emission before 1 May also have influence on the dust concentration during 1 May to 7 May. To study the dust simulation sensitivity to dust emission and dry deposition schemes, we run 6 experiments with two different dust emission schemes and three dry deposition schemes (See Table 3). The corresponding model configuration for dust emission and dry deposition processes of the six experiments also listed in Table 3.



230 2.5 Measurements

Hourly surface observed PM₁₀ is used to compare with the simulated PM₁₀ from WRF-Chem. In China, hourly surface PM₁₀ concentrations were collected from more than 1000 environmental monitoring stations maintained by the Ministry of Environmental Protection (MEP). The hourly PM₁₀ data from 1 May to 7 May, 2017 were downloaded from <http://beijingair.sinaapp.com/>. We collocated the PM₁₀ data to WRF-Chem simulation grids to evaluate model performance
235 with different configurations.

Daily aerosol optical depth (AOD) from Moderate Resolution Imaging Spectroradiometer (MODIS) is used to compare with our simulated AOD from WRF-Chem. The MODIS onboard Aqua satellite was launched by the NASA in 2002 and Aqua is a part of A-Train satellite constellation. To compare modelled AOD with observations, we use AOD retrievals at 550 nm from MODIS AOD products on Aqua with daily gridded data at a resolution of 1°×1° (MYD08_D3, Collection 6, combined dark
240 target and deep blue AOD). The MODIS Aqua collection daily MYD08_D3 files were obtained from <https://ladsweb.nascom.nasa.gov>. As Aqua passes through every region of Earth at 13:30 p.m. local time, we extract the model simulation results at 13:00 p.m. to compare with the daily MODIS AOD.

3 Results

3.1 Dust simulation sensitivity to dust emission schemes

245 In this section, we examine the changes of the simulated dust loading using different dust emission schemes. Figure 1 shows simulated mean dust loading for six experiments over the 7-day simulation period 1-7 May, 2017. When using the same dry deposition scheme (BS95, PE92 or Z01), different dust emission schemes give very different dust spatial distribution. Compared with the Shao2011 scheme, GOCART has higher dust loading over the Taklimakan desert but has relatively lower dust loading over the Gobi Desert, the south of Outer Mongolia and most parts of northern China. The difference of the
250 spatial distribution of dust loading is mainly caused by the different spatial distribution of dust emission flux from dust emission schemes, as shown in Fig. 2. As the dust emission before 1 May also have influence on the dust loading during 1



May to 7 May, the total dust emission from 28 April to 7 May are analyzed. The total dust emission from 00:00 UTC 28 April to 23:00 UTC 7 May over GD from GOCART and Shao2011 are 5.42 Tg and 13.62 Tg, respectively. The total dust emission from 00:00 UTC 28 April to 23:00 UTC 7 May over TD from GOCART and Shao2011 are 7.12 Tg and 2.73 Tg respectively (Fig. 2c). Over Gobi Desert, Shao2011 scheme has higher dust emission than GOCART; while over Taklimakan Desert, GOCART scheme has higher dust emission than Shao2011 (Fig. 2c).

The first column of Fig. 3 shows the spatial distribution of friction velocity, threshold friction velocity, the difference between friction velocity and threshold friction velocity and the dust emission flux from Shao2011 at 06:00 UTC on 3 May. The areas where the friction velocity is greater than the threshold friction velocity is mainly located in the west inner Mongolia and the south of Outer Mongolia (Fig. 3e). This is consistent with Fig. 3g. When the friction velocity is larger than threshold friction velocity, dust can be emitted from the surface. The second column of Fig. 3 shows the spatial distribution of wind speed at 10 meters, threshold velocity, the difference between wind speed at 10 meters and threshold velocity and the dust emission flux from the GOCART dust emission scheme. Different from Shao2011, the dust emission regions from GOCART are not only determined by wind speed, but also constrained by erodibility factor (Eq. (1)). From Fig. 3f, the threshold velocity is much smaller than the wind speed at 10 meters in most areas. In these areas, GOCART use Eq. (1) to calculate the dust emission flux, and the source function S depends on the erodibility factor. The dust emission flux in GOCART is directly scaled by erodibility factor. Figure 4 shows the erodibility factor which describes the fraction of erodible surface in each grid cell. As shown in Fig. 3h, dust emission occurs where the wind speed is high and the erodibility factor is larger than 0. So the difference of dust emission between GOCART and Shao2011 is mainly due to the difference of threshold conditions for dust emission and the difference of formulas and parameters for calculating dust emission flux.

Over Taklimakan desert (TD), Shao2011 produces lower dust emission flux than GOCART. As mentioned by Wu and Lin (2014), there are two possible reasons for this. One is that dust generated by the intermittent turbulence is not considered in Shao2011 scheme. Dust can be generated by the intermittent turbulence rather than by the mean wind shear when the wind speed is low (Klose and Shao, 2012). While GOCART uses the erodibility factor and the empirical formula to calculate the dust emission flux, dust can be emitted where the wind speed is relatively low. Another reason may be the incorrect soil particle size distribution over TD. The incorrect soil particle size distribution can lead to the unreasonable dust emission flux



in Shao2011 over TD. Over Gobi Desert (GD), the GOCART scheme has lower dust emission than the Shao2011 scheme. As mentioned by Su and Fung (2015), the erodibility factor over Gobi Desert is highly underestimated and need to be improved for the GOCART dust emission scheme.

280 We note that, the Shao2011 dust emission scheme we used in this study is based on WRF-Chem v3.9 with some modifications from WRF-Chem v3.7.1 as documented in Appendix B. The modified Shao2011 simulates better dust loading than the original Shao2011 scheme in WRF-Chem v3.9 (not shown). Simulated dust emission fluxes can differ a lot between two versions of the Shao2011 scheme in WRF-Chem v3.9 and WRF-Chem v3.7.1, which is mainly caused by different soil particle size distributions in two versions. The differences of Shao2011 among different WRF-Chem versions are documented
285 in Appendix B.

3.2 Dust simulation sensitivity to dry deposition schemes

In this section, we analyze dust simulation sensitivity to different dry deposition schemes using the six experiments. For simulated dust loading using the GOCART dust emission scheme (the first row in Fig. 1), compared to the BS95 dry deposition scheme, PE92 and Z01 produce higher dust loading over the dust source regions and remote regions. The relative
290 difference of mean dust loading from PE92 and Z01 relative to BS95 is 20% and 59% respectively. As for the simulated dust loading using the Shao2011 dust emission scheme (the second row in Fig. 1), PE92 and Z01 schemes also produce higher dust loading than BS95 scheme, and the relative difference to BS95 is 72% and 116% respectively. This indicates that dust simulation is very sensitive to dry deposition schemes.

Figure 5a shows the modeled dry deposition velocity over desert surface. As desert dust mass is mainly concentrated in the
295 large particle size range, our dry deposition analysis focuses on the coarse mode (near the reference diameter marked as colored dots in Fig. 5). BS95 produces larger V_d than PE92 and Z01 in the coarse aerosol mode. Larger V_d leads to larger dry deposition and thus lower dust loading, consistent with the lower simulated dust loading from the BS95 scheme discussed above (Fig. 1). In Eq. (3), the dry deposition velocity is comprised of gravitational velocity, aerodynamic resistance and surface resistance. The diversity of different dry deposition schemes mainly comes from the way to
300 parameterize surface resistance, and differences from gravitational settling and aerodynamics resistance are small (not



shown), consistent with previous studies (e.g., Bergametti et al., 2018). Figure 5b shows the surface resistance from different schemes as a function of particle diameter (D_p). In the coarse aerosol mode, Z01 produces the largest surface resistance, followed by PE92 and BS95. Larger surface resistance causes smaller dry deposition velocity in Z01, thus larger dust concentration as shown in Fig. 1.

305 The surface collection efficiency is comprised of Brownian diffusion, impaction, and interception and is corrected for particle rebound (see Eq. (10)). Collection from Brownian diffusion is most important for the smaller particles while collection from impaction and interception play a more important role for large particles in surface collection processes. Figure 5c shows the surface collection efficiency from impaction (E_{IM}) from different schemes as a function of particle diameter. Impaction occurs when there are changes in the direction of airflow, and their inertia carries them across the
310 sublayer to the surface (Seinfeld and Pandis, 2006). BS95 gives the largest E_{IM} and Z01 gives the smallest. Based on field observation data, Slinn (1982) used a semi-empirical fit for smooth surface (Eq. (7)), and Binkowski and Shankar (1995) adopted this formula for E_{IM} and used it for all land surface types. Peters and Eiden (1992) uses Eq. (17) to describe E_{IM} , with α equals to 0.8 and β equals to 2 to get the best fit for the data collected over a spruce forest. In Zhang et al. (2001) scheme, α varies with LUC and β is chosen as 2. For BS95 and PE92, the formula of E_{IM} is derived from a specific land
315 surface type, but they have been applied to all land surface types in WRF-Chem. This may lead to large uncertainties for dry deposition over the whole domain with different surface types. As E_{IM} of Z01 varies with LUC, Z01 may have a better physical treatment of E_{IM} than the other two dry deposition schemes.

Figure 5d shows the surface collection efficiency from interception (E_{IN}). Collection from interception occurs when particles moving with the mean flow and the distance between an obstacle and particle center is less than half of the diameter, and
320 E_{IN} therefore depends on the particle diameter and the characteristic radius of the collectors (Seinfeld and Pandis, 2006). E_{IN} is important for large particles on hairs at the leaf surface, and is negligible over non-vegetated surface such as the desert surface we analyzed here (Chamberlain, 1967; Slinn, 1982; Zhang et al., 2001). In BS95, the effect of interception is not considered. In the original PE92 scheme as described in Peters and Eiden (1992), E_{IN} is also not considered. But in the PE92 scheme used in WRF-Chem, E_{IN} increases with particle diameter as in Eq. (12). In Z01, the effect of interception is
325 considered as Eq. (20) over vegetated surface and is not considered for non-vegetated surface (as shown in Fig. 5d over



desert surface type). The parameterization of E_{IN} partially results in the difference of surface resistance between PE92 and the other two dry deposition schemes.

Figure 5e shows the rebound factor from different dry deposition schemes. Rebound and resuspension have long been recognized as a mechanism by which the surface can act as sources of particles (Pryor et al., 2008). Due to limited knowledge on particle rebound and resuspension processes, most dry deposition models adopted the form of the rebound effect as $R = e^{-b\sqrt{St}}$ suggested by Slinn (1982) (Zhang and Shao, 2014; Zhang et al., 2001), while some dry deposition schemes do not include the rebound effect with $R=1.0$ (Binkowski and Shankar, 1995; Petroff and Zhang, 2010; Zhang and He, 2014). BS95 does not consider the rebound effect. b is equal to 2.0 for PE92 scheme and 1.0 for Z01 scheme. Another difference between PE92 and Z01 is the threshold particle diameter for including the rebound effect. Rebound effect is included for PE92 when particles are larger than $0.625 \mu\text{m}$ and for Z01 when particles are larger than $2.5 \mu\text{m}$. In summary, the smaller E_{IM} and rebound factor lead to larger R_S in Z01, while the larger E_{IM} leads to smaller R_S in BS95, and the moderate E_{IM} and rebound effect give a moderate R_S for PE92.

Stokes number is the ratio of the particle stop distance to the characteristic length of the flow, and it describes the ability of particles to adopt the fluid velocity (Pryor et al., 2008; Seinfeld and Pandis, 2006). Over smooth surfaces, the formula of St for BS95 and Z01 is the same, as shown in Eq. (19). In PE92, St is calculated using Eq. (14), which is similar to the formula used in Slinn (1982). Figure 5f shows the Stokes number from different dry deposition schemes. BS95 and Z01 schemes give a larger St than PE92. Stokes number is used to calculate both R and E_{IM} . The difference of Stokes number and the different formulas of R and E_{IM} lead to the different R and E_{IM} among different dry deposition schemes (Fig. 5c and 5e).

Our discussion indicates that Z01 has a better physical treatment of dry deposition velocity, as Z01 considers the rebound effect and E_{IM} changes with LUC. The Z01 scheme has also been documented to agree better with measured dry deposition fluxes and dry deposition velocity (e.g., Zhang et al., 2012; Connan et al., 2018). Zhang et al. (2012) compared the dry deposition fluxes measured at five sites in Taiwan with the modeled dry deposition fluxes and found that the measured dry deposition fluxes can be reproduced reasonably well using the Z01 scheme. Connan et al. (2018) conducted experimental campaigns on-site to determine dry deposition velocity of aerosols and found that the Z01 scheme is most suitable for operational use in the size range $0.2\text{-}10 \mu\text{m}$. All these indicate that the Z01 dry deposition scheme is better than other two dry



deposition schemes.

3.3 Comparisons with observations

To better evaluate the performance of different experiments, we compared the model results with observations. Figure 6 shows hourly observed PM_{10} concentrations over observational sites at 02:00 UTC on 4 May, 2017 (10:00 Beijing Time (BJT) on 4 May, 2017). Very high PM_{10} values ($> 1000 \mu g m^{-3}$) are observed in northern China. Figure 7 compares simulated PM_{10} in six experiments with observed PM_{10} . During the comparison, the observational sites closest to the model grids are paired up. The correlation coefficients (R), root mean square errors (RMSE) between model and observations, and the mean simulated and observed PM_{10} for all the sites over the five regions during the 7-day period 1-7 May are marked in Fig. 7. The simulated PM_{10} of all the six experiments have obviously underestimated the observations. Among all these experiments, GOBS95 has the lowest average PM_{10} concentration, with a value of $26.45 \mu g m^{-3}$, and S11Z01 has the largest one, with a value of $105.17 \mu g m^{-3}$, the closest one to the observed mean value of $172.70 \mu g m^{-3}$. S11Z01 gives a large R of 0.77 and the smallest RMSE of 96.14 compared to other experiments. Table 4 shows the R and RMSE between the model and observations for PM_{10} for six experiments over five sub regions and over whole China. Over TD, GOBS95 gives the largest R and smallest RMSE. Over GD, GOZ01 and S11Z01 gives a better performance compared with other experiments. For other regions (NCP, NEP and YR), S11Z01 gives a relatively larger R and smallest RMSE. For all the stations in total, S11Z01 gives a larger R of 0.83 and the smallest RMSE of 82.98. Overall, the S11Z01 experiment has the best performance for simulating this dust storm.

Figure 8 shows the MODIS observed daily mean AOD and WRF-Chem simulated AOD on 4 May for six experiments. For strong dust storms like the one we examined here, dust particles contribute the most to AOD, and AOD therefore can represent the dust loading in the atmosphere. To match the MODIS AOD observation time, simulated AOD at 13:00 p.m. local time is used for comparison. For each $1^\circ \times 1^\circ$ grid with observed AOD from MODIS, the average value of simulated AOD from WRF-Chem in this grid is calculated. The simulated AOD already collocated with MODIS AOD in Fig. 8. Extremely high AOD values were observed in the northern China from MODIS (Fig. 8a). When using GOCART dust emission scheme, AOD is highly underestimated over most regions except over Taklimakan Desert (Fig. 8b, 8c, 8d). When



375 using Shao2011 dust emission scheme coupled with BS95 or PE92 dry deposition scheme (Fig. 8e, 8f), AOD is also underestimated over most regions, but with relatively larger AOD than using GOCART dust emission scheme. AOD from the S11Z01 experiment is the closest one to the MODIS observed AOD (Fig. 8g). For a more quantitative comparison, we collocated the simulated AOD with observed MODIS AOD over the 7-day simulation period 1-7 May, 2017. Table 5 shows the correlation coefficient (R) and root mean square error (RMSE) between the model and observed AOD for six
380 experiments during 1-7 May. Overall, S11Z01 experiment gives a larger correlation coefficient and the RMSE is almost the same among different experiments, the correlation coefficient is still lower than 0.5. The low correlation may partly come from the spatial and temporal limitation of satellites and the difficulties to retrieve aerosol in the vicinity of clouds for satellites.

In summary, both ground and satellite observations indicate that the S11Z01 experiment yields the best performance in
385 simulating this dust storm. As we discussed in Sect. 3.2, the Z01 dry deposition scheme indeed has a better physical treatment and performs better than some other dry deposition schemes.

4 Summary and discussion

In this study, we analyzed the dust simulation sensitivity to different dust emission schemes and dry deposition schemes. In order to compare different dust emission schemes, the Shao2011 dust emission scheme has been implemented into the
390 MOSAIC aerosol scheme in WRF-Chem v3.9. Six model experiments were conducted to simulate the dust storm in May 2017 over East Asia, with two dust emission schemes (GOCART and Shao2011) and three dry deposition schemes (BS95, PE92 and Z01). The simulation results of different experiments were evaluated against surface and satellite observations.

Our results show that dust loading is very sensitive to different dry deposition schemes. The relative difference of dust loading in different experiments range from 20%-116% when using different dry deposition schemes. The difference of dry deposition
395 velocity in different dry deposition schemes comes from the parameterization of surface resistance, and difference in surface resistance mainly comes from the parameterization of collection efficiency from impaction and rebound effect. In addition, different dust emission schemes result in different spatial distribution of dust loading, as dust emission fluxes in dust source regions differ a lot among different dust emission schemes, which is mainly attributed to differences in the threshold conditions



for dust emission and in formulas and parameters for calculating dust emission flux. We noted that, the Shao2011 dust
400 emission scheme is different among different WRF-Chem versions, and simulated dust emission fluxes in WRF-Chem v3.9
and WRF-Chem v3.7.1 can differ a lot, which is mainly caused by differences in soil particle size distributions used in two
versions (see Appendix B).

Compared with both surface PM₁₀ station observations and MODIS AOD, the Shao2011 dust emission scheme coupled with
the Z01 dry deposition scheme produces the best simulation for the dust storm in East Asia. Our analysis indicates Z01
405 accounts for the rebound effect and E_{IM} changes with LUC and therefore has a better physical treatment of dry deposition
velocity than the two other dry deposition schemes. Previous studies have also shown that the Z01 scheme agrees better with
measured dry deposition fluxes and dry deposition velocity (e.g., Zhang et al., 2012; Connan et al., 2018). The Shao2011 dust
emission scheme has larger dust emission fluxes than GOCART dust emission scheme over Gobi Desert, and the transport of
dust emitted from Gobi Desert is the most important source of dust weather in northern China. The Shao2011 scheme has also
410 been documented to give better performance in dust simulation over East Asia (Su and Fung, 2015).

This study highlights the importance of dry deposition process in dust simulation. Future studies on dust simulation should
pay attention to improve dry deposition schemes as well as the dust emission schemes. Additional field measurements of dry
deposition process and comparisons with model results are required to reduce the uncertainties on dust simulation.

Appendix A: Description of the Shao2011 dust emission scheme

415 Here we describe the Shao2011 dust emission scheme in more detail as a supplement to the Sect. 2.2.2 of this article. The
saltation flux $Q(d_s)$ in Eq. (2) is calculated as:

$$Q(d_s) = (1 - c_f)c_0 \frac{\rho}{g} u_*^3 \left(1 - \frac{u_{*t}}{u_*}\right) \left(1 + \frac{u_{*t}}{u_*}\right)^2 \quad (\text{A1})$$

where c_f is the fraction of vegetation cover, $(1-c_f)$ means the fraction of erodible surface area, c_0 is a coefficient. u_{*t}
is the threshold friction velocity, u_* is the friction velocity. When u_* is larger than u_{*t} , it calculates the dust emission flux.

420 Before WRF-Chem v4.0, there is a bug in calculating the saltation flux $Q(d_s)$ in Shao2011. They miscalculate the last term as
 $\left(1 + \left(\frac{u_{*t}}{u_*}\right)^2\right)$ in WRF-Chem codes (LeGrand et al., 2019). In WRF-Chem v4.0 and later versions, they fixed this bug and we



also fixed this bug in our simulations.

The threshold friction velocity u_{*t} is calculated as:

$$u_{*t} = u_{*t0} f_{\lambda} f_{\theta} \dots \quad (\text{A2})$$

425 where u_{*t0} is the ideal threshold friction velocity when soil is dry, bare and free of crust and salt, f_{λ} is the correction functions for surface roughness, f_{θ} is the correction functions for soil moisture. The ideal threshold friction u_{*t0} is calculated as:

$$u_{*t0} = \sqrt{a_1 \frac{\rho_p}{\rho_a} g d + \frac{a_2}{\rho_a d}} \quad (\text{A3})$$

where a_1 and a_2 are constant. ρ_p and ρ_a are particle and air density. d is the particle diameter.

430 The correction functions for surface roughness f_{λ} is calculated as:

$$f_{\lambda} = [(1 - m\sigma\lambda)(1 + m\beta\lambda)]^{\frac{1}{2}} \quad (\text{A4})$$

where m is a constant, σ is the ratio of roughness-element basal area to frontal area, λ is the frontal area index, β is the ratio of the drag coefficient of an isolated roughness element on the surface to the drag coefficient of the substrate surface itself.

435 The mass fraction of free dust η_{mi} is calculated as:

$$\eta_{mi} = \int_{d - \frac{\Delta d_i}{2}}^{d + \frac{\Delta d_i}{2}} p_m(d) \delta d \quad (\text{A5})$$

where $p_m(d)$ is the minimally disturbed particle-size distribution, which is regarded as a composite of several log-normal distribution, $p_m(d)$ is expressed as:

$$p_m(d) = \frac{1}{d} \sum_{j=1}^J \frac{w_j}{\sqrt{2\pi}\sigma_j} \exp\left(-\frac{(\ln d - \ln D_j)^2}{2\sigma_j^2}\right) \quad (\text{A6})$$

440 soil samples collected from experiment sites are used to determine the particle size distribution.

Appendix B: The Shao2011 dust emission scheme in different versions of WRF-Chem

As we noted in Sect. 3.1, the Shao2011 scheme in different versions of WRF-Chem can produce significantly different dust



emission fluxes. Here we document differences in Shao2011 among different WRF-Chem versions:

1. The first difference is c_0 . c_0 is a coefficient used to calculate the saltation flux as in Eq. (A1). In versions before
445 WRF-Chem v3.8, c_0 is equal to 0.5; in WRF-Chem v3.8 and later versions, c_0 is equal to 2.3 (Table B1).
2. The second difference is β . β is a coefficient used to calculate the correction function for surface roughness f_λ in Eq.
(A4). In versions before WRF-Chem v3.8, β is 90; in WRF-Chem v3.8 and later versions, β is 200 (Table B1).
3. The third difference is caused by the minimally disturbed particle-size distribution $p_m(d)$ (see Eq. (A6)). $p_m(d)$ is
450 used to calculate the free dust fraction η_{mi} (see Eq. (A5)). Free dust fraction is the fraction of dust that has lower
enough binding energy so that it can be easily lifted from the surface by either aerodynamic forces or mechanical
abrasion (Shao, 2001). The η_{mi} is used to calculate the dust emission rate in Eq. (2). 12 soil types are included in all
WRF-Chem versions. In WRF-Chem v3.8 and later versions, each soil type has a corresponding $p_m(d)$ as listed in
Table B1 from Shao et al. (2010); in versions before WRF-Chem v3.8, there are only four $p_m(d)$ as listed in Table 1
455 from Shao (2004) for 12 soil types (Fig. B1). For example, (f) sand and (g) loamy sand soil types use the same free dust
fraction distribution in versions before WRF-Chem v3.8. As shown in Table B2, the loam and clay loam are the two soil
types with the largest percentage, while the other soil types account for a very small percentage. From Fig. B1c and Fig.
B1e, for loam and clay loam soil types, the free dust fraction is so small in the particle size range 0-10 μm in
WRF-Chem v3.8 and later versions, almost all close to 0; while in the versions before WRF-Chem v3.8, the free dust
fraction is relatively high. In different WRF-Chem versions, the total saltation flux Q is the same, but dust emission flux
460 $F(d_i)$ is different due to different free dust fraction (see Eq. (2)). With smaller free dust fraction, the dust emission flux
is smaller in WRF-Chem v3.8 and later versions.

To examine the importance of these changes, we run four experiments to quantify the contribution of each factor (Table B3).
For control run, c_0 is 2.3, β is 200 and $p_m(d)$ has 12 distributions based on WRF-Chem v3.8 or later versions. For case1
experiment, β is changed to 90, the one used in WRF-Chem v3.7.1 and all other parameters are kept the same as in control
465 run. The dust emission of case1 is 1.35 times higher than the control run. For case2 experiment, c_0 is changed to 0.5, the
one used in WRF-Chem v3.7.1, and all other parameters remain the same as in control run. The dust emission of case2 is
twenty-one percent of the dust emission of the control run. For case3 experiment, $p_m(d)$ is adopted from WRF-Chem



v3.7.1 and has four distributions, and all other parameters remain the same as in control run. The dust emission of case3 is 13 times higher than the control run. This indicates that the difference of dust emission between different versions of Shao2011 scheme is mainly caused by the change of $p_m(d)$. As $p_m(d)$ is determined by soil particle size distribution, this also highlights the need to improve the accuracy of soil texture.

We should mention that the Shao2011 dust emission scheme we used in this study is based on WRF-Chem v3.9 with the soil particle size distribution from WRF-Chem v3.7.1, which simulates better dust loading compared with observations. Compared with the original Shao2011 scheme in WRF-Chem v3.9, the total dust emission simulated in our experiments during 1-7 May is 13 times higher.

Code availability

The source code of WRF-Chem is available at http://www2.mmm.ucar.edu/wrf/users/download/get_sources.html (last access: 31 October 2019). The modified WRF-Chem v3.9 with Shao2011 dust emission scheme implemented in MOSAIC aerosol scheme is available upon request to the corresponding author.

Data availability

The 6-hourly National Center for Environmental Prediction Final (NECP FNL) Operational Global Analysis data at a resolution of $1^\circ \times 1^\circ$ can be obtained from: <https://rda.ucar.edu/> (last access: 31 October 2019). The observed PM10 data is collected from the National air quality real time release platform at: <http://106.37.208.233:20035/> (last access: 31 October 2019). The historical data of air quality used in this study can be downloaded from: <http://beijingair.sinaapp.com/> (last access: 31 October 2019). Daily MYD08_D3 files from the MODIS onboard Aqua satellite can be obtained from <https://ladsweb.nascom.nasa.gov> (last access: 31 October 2019).



Author contributions

MW and YZ conceived the idea and designed the model experiments. YZ performed the simulations, conducted the analysis and wrote the manuscript. CZ and SC provided guideline for the dust simulations in WRF-Chem and helped in the
490 interpretation of the results. XH and ZL provided guideline for the WRF-Chem simulations and contributed to the model experiments design. YG helped in the PM10 data processing and usage. Everyone edited the manuscript.

Competing interests

The authors declare that they have no conflict of interest.

Acknowledgements

495 This work is supported by the Minister of Science and Technology of China (2016YFC0200503 and 2017YFA0604002) and by the National Natural Science Foundation of China (41575073, 41621005 and 91744208). This research is also supported by the Collaborative Innovation Center of Climate Change, Jiangsu Province. Chun Zhao is supported by the Natural Science Foundation of China NSFC (41775146) and the Fundamental Research Funds for the Central Universities.

References

- 500 Abuduwaili, J., LIU, D. and WU, G.: Saline dust storms and their ecological impacts in arid regions, *J. Arid Land*, 2(2), 144–150, doi:10.3724/sp.j.1227.2010.00144, 2010.
- Bergametti, G., Marticorena, B., Rajot, J. L., Foret, G., Alfaro, S. C. and Laurent, B.: Size-Resolved Dry Deposition Velocities of Dust Particles: In Situ Measurements and Parameterizations Testing, *J. Geophys. Res. Atmos.*, 123(19), 11,080-11,099, doi:10.1029/2018JD028964, 2018.
- 505 Binkowski, F. S. and Shankar, U.: The Regional Particulate Matter Model: 1. Model description and preliminary results, *J.*



- Geophys. Res., 100(D12), 26191, doi:10.1029/95JD02093, 1995.
- Chamberlain, A. C.: Transport of Lycopodium spores and other small particles to rough surfaces, Proc. R. Soc. London. Ser. A. Math. Phys. Sci., 296(1444), 45–70, doi:10.1098/rspa.1967.0005, 1967.
- Chen, F. and Dudhia, J.: Coupling an Advanced Land Surface–Hydrology Model with the Penn State–NCAR MM5 Modeling System. Part I: Model Implementation and Sensitivity, Mon. Weather Rev., 129(4), 569–585, doi:10.1175/1520-0493(2001)129<0569:CAALSH>2.0.CO;2, 2001.
- Chen, S., Huang, J., Zhao, C., Qian, Y., Leung, L. R. and Yang, B.: Modeling the transport and radiative forcing of taklimakan dust over the tibetan plateau: A case study in the summer of 2006, J. Geophys. Res. Atmos., 118(2), 797–812, doi:10.1002/jgrd.50122, 2013.
- 515 Chen, S., Huang, J., Qian, Y., Zhao, C., Kang, L., Yang, B. and Wang, Y.: An Overview of Mineral Dust Modeling over East Asia, , 31(August), doi:10.1007/s13351-017-6142-2.1.Introduction, 2017.
- Chen, S., Zhang, X., Lin, J., Huang, J., Zhao, D., Yuan, T., Huang, K., Luo, Y., Jia, Z., Zang, Z., Qiu, Y. and Xie, L.: Fugitive Road Dust PM_{2.5} Emissions and Their Potential Health Impacts, Environ. Sci. Technol., 53, 8455–8465, doi:10.1021/acs.est.9b00666, 2019.
- 520 Connan, O., Pellerin, G., Maro, D., Damay, P., H ébert, D., Roupsard, P., Rozet, M. and Laguionie, P.: Dry deposition velocities of particles on grass : Field experimental data and comparison with models, J. Aerosol Sci., 126(July), 58–67, doi:10.1016/j.jaerosci.2018.08.004, 2018.
- Creamean, J. M., Suski, K. J., Rosenfeld, D., Cazorla, A., Demott, P. J., Sullivan, R. C., White, A. B., Ralph, F. M., Minnis, P., Comstock, J. M., Tomlinson, J. M. and Prather, K. A.: Dust and Biological Aerosols, , 339(March), 1572–1579, 2013.
- 525 Demott, P. J., Prenni, A. J., Liu, X., Kreidenweis, S. M., Petters, M. D., Twohy, C. H. and Richardson, M. S.: Predicting global atmospheric ice nuclei distributions and their impacts on climate, , 1–6, doi:10.1073/pnas.0910818107, 2010.
- Ginoux, P., Chin, M., Tegen, I., Prospero, J. M., Holben, B., Dubovik, O. and Lin, S.-J.: Sources and distributions of dust aerosols simulated with the GOCART model, J. Geophys. Res. Atmos., 106(D17), 20255–20273, doi:10.1029/2000JD000053, 2001.
- 530 Giorgi, F.: A particle dry-deposition parameterization scheme for use in tracer transport models, J. Geophys. Res., 91(D9), 9794, doi:10.1029/JD091iD09p09794, 1986.
- Giorgi, F.: Dry deposition velocities of atmospheric aerosols as inferred by applying a particle dry deposition parameterization to a general circulation model, Tellus B, 40B(1), 23–41, doi:10.1111/j.1600-0889.1988.tb00210.x, 1988.
- Grell, G. A. and Freitas, S. R.: A scale and aerosol aware stochastic convective parameterization for weather and air quality modeling, Atmos. Chem. Phys., 14(10), 5233–5250, doi:10.5194/acp-14-5233-2014, 2014.
- 535 Grell, G. A., Peckham, S. E., Schmitz, R., McKeen, S. A., Frost, G., Skamarock, W. C. and Eder, B.: Fully coupled “online” chemistry within the WRF model, Atmos. Environ., 39(37), 6957–6975, doi:10.1016/j.atmosenv.2005.04.027, 2005.



- Guo, P., Yu, S., Wang, L., Li, P., Li, Z., Mehmood, K., Chen, X., Liu, W., Zhu, Y., Yu, X., Alapaty, K., Lichtfouse, E., Rosenfeld, D. and Seinfeld, J. H.: High-altitude and long-range transport of aerosols causing regional severe haze during extreme dust storms explains why afforestation does not prevent storms, *Environ. Chem. Lett.*, 1–8, doi:10.1007/s10311-019-00858-0, 2019.
- Hansen, J., Sato, M. and Ruedy, R.: Radiative forcing and climate response, *J. Geophys. Res. Atmos.*, 102(D6), 6831–6864, doi:10.1029/96JD03436, 1997.
- Hicks, B. B., Saylor, R. D. and Baker, B. D.: Dry deposition of particles to canopies-A look back and the road forward, *J. Geophys. Res. Atmos.*, 121(24), 14,691–14,707, doi:10.1002/2015JD024742, 2016.
- Hofer, J., Althausen, D., Abdullaev, S. F., Makhmudov, A. N., Nazarov, B. I., Schettler, G., Engelmann, R., Baars, H., Fomba, K. W., Müller, K., Heinold, B., Kandler, K. and Ansmann, A.: Long-term profiling of mineral dust and pollution aerosol with multiwavelength polarization Raman lidar at the Central Asian site of Dushanbe, Tajikistan: Case studies, *Atmos. Chem. Phys.*, 17(23), 14559–14577, doi:10.5194/acp-17-14559-2017, 2017.
- Hong, S.-Y., Noh, Y. and Dudhia, J.: A New Vertical Diffusion Package with an Explicit Treatment of Entrainment Processes, *Mon. Weather Rev.*, 134(9), 2318–2341, doi:10.1175/MWR3199.1, 2006.
- Huneus, N., Schulz, M., Balkanski, Y., Griesfeller, J., Prospero, J., Kinne, S., Bauer, S., Boucher, O., Chin, M., Dentener, F., Diehl, T., Easter, R., Fillmore, D., Ghan, S., Ginoux, P., Grini, A., Horowitz, L., Koch, D., Krol, M. C., Landing, W., Liu, X., Mahowald, N., Miller, R., Morcrette, J.-J., Myhre, G., Penner, J., Perlwitz, J., Stier, P., Takemura, T. and Zender, C. S.: Global dust model intercomparison in AeroCom phase I, *Atmos. Chem. Phys.*, 11(15), 7781–7816, doi:10.5194/acp-11-7781-2011, 2011.
- Iacono, M. J., Delamere, J. S., Mlawer, E. J., Shephard, M. W., Clough, S. A. and Collins, W. D.: Radiative forcing by long-lived greenhouse gases: Calculations with the AER radiative transfer models, *J. Geophys. Res. Atmos.*, 113(13), 2–9, doi:10.1029/2008JD009944, 2008.
- Jiménez-Guerrero, P., Pérez, C., Jorba, O. and Baldasano, J. M.: Contribution of Saharan dust in an integrated air quality system and its on-line assessment, *Geophys. Res. Lett.*, 35(3), 1–6, doi:10.1029/2007GL031580, 2008.
- Kang, J. Y., Yoon, S. C., Shao, Y. and Kim, S. W.: Comparison of vertical dust flux by implementing three dust emission schemes in WRF / Chem, , 116(May), 1–18, doi:10.1029/2010JD014649, 2011.
- Khan, T. R. and Perlinger, J. A.: Evaluation of five dry particle deposition parameterizations for incorporation into atmospheric transport models, *Geosci. Model Dev.*, 10(10), 3861–3888, doi:10.5194/gmd-10-3861-2017, 2017.
- Klose, M. and Shao, Y.: Stochastic parameterization of dust emission and application to convective atmospheric conditions, *Atmos. Chem. Phys.*, 12(16), 7309–7320, doi:10.5194/acp-12-7309-2012, 2012.
- Kok, J. F., Ridley, D. A., Zhou, Q., Miller, R. L., Zhao, C., Heald, C. L., Ward, D. S., Albani, S. and Haustein, K.: Smaller desert dust cooling effect estimated from analysis of dust size and abundance, , doi:10.1038/NGEO2912, 2017.



- 570 LeGrand, S. L., Polashenski, C., Letcher, T. W., Creighton, G. A., Peckham, S. E. and Cetola, J. D.: The AFWA dust emission scheme for the GOCART aerosol model in WRF-Chem v3.8.1, *Geosci. Model Dev.*, 12(1), 131–166, doi:10.5194/gmd-12-131-2019, 2019.
- Marticorena, B. and Bergametti, G.: Modeling the atmospheric dust cycle: 1. Design of a soil-derived dust emission scheme, *J. Geophys. Res.*, 100(D8), 16415, doi:10.1029/95JD00690, 1995.
- 575 Morrison, H., Thompson, G. and Tatarskii, V.: Impact of Cloud Microphysics on the Development of Trailing Stratiform Precipitation in a Simulated Squall Line: Comparison of One- and Two-Moment Schemes, *Mon. Weather Rev.*, 137(3), 991–1007, doi:10.1175/2008mwr2556.1, 2008.
- Ozer, P., Laghdaf, M. B. O. M., Lemine, S. O. M. and Gassani, J.: Estimation of air quality degradation due to Saharan dust at Nouakchott, Mauritania, from horizontal visibility data, *Water, Air, Soil Pollut.*, 178(1–4), 79–87, doi:10.1007/s11270-006-9152-8, 2007.
- 580 Peters, K. and Eiden, R.: Modelling the dry deposition velocity of aerosol particles to a spruce forest, *Atmos. Environ. Part A. Gen. Top.*, 26(14), 2555–2564, doi:10.1016/0960-1686(92)90108-W, 1992.
- Petroff, A. and Zhang, L.: Development and validation of a size-resolved particle dry deposition scheme for application in aerosol transport models, *Geosci. Model Dev.*, 3(2), 753–769, doi:10.5194/gmd-3-753-2010, 2010.
- 585 Petroff, A., Mailliat, A., Amielh, M. and Anselmet, F.: Aerosol dry deposition on vegetative canopies. Part I: Review of present knowledge, *Atmos. Environ.*, 42(16), 3625–3653, doi:10.1016/j.atmosenv.2007.09.043, 2008.
- Prospero, J. M., Landing, W. M. and Schulz, M.: African dust deposition to Florida: Temporal and spatial variability and comparisons to models, *J. Geophys. Res.*, 115(D13), D13304, doi:10.1029/2009JD012773, 2010.
- Pryor, S. C., Gallagher, M., Sievering, H., Larsen, S. E., Barthelmie, R. J., Birsan, F., Nemitz, E., Rinne, J., Kulmala, M., Grönholm, T., Taipale, R. and Vesala, T.: A review of measurement and modelling results of particle atmosphere–surface exchange, *Tellus B Chem. Phys. Meteorol.*, 60(1), 42–75, doi:10.1111/j.1600-0889.2007.00298.x, 2008.
- 590 Ruijrok, W., Davidson, C. I. and Nicholson, K. W.: Dry deposition of particles, *Tellus B Chem. Phys. Meteorol.*, 47(5), 587–601, doi:10.3402/tellusb.v47i5.16074, 1995.
- Seinfeld, J. H. and Pandis, S. N.: *Atmospheric chemistry and physics: from Air Pollution to Climate Change*, Second edition, A wiley-Interscience Publication, Hoboken, New Jersey, 2006.
- 595 Shao, Y.: A model for mineral dust emission, *J. Geophys. Res. Atmos.*, 106(D17), 20239–20254, doi:10.1029/2001JD900171, 2001.
- Shao, Y.: Simplification of a dust emission scheme and comparison with data, *J. Geophys. Res. D Atmos.*, 109(10), 1–6, doi:10.1029/2003JD004372, 2004.
- 600 Shao, Y., Fink, A. H. and Klose, M.: Numerical simulation of a continental-scale Saharan dust event, *J. Geophys. Res.*, 115(D13), D13205, doi:10.1029/2009JD012678, 2010.



- Shao, Y., Ishizuka, M., Mikami, M. and Leys, J. F.: Parameterization of size-resolved dust emission and validation with measurements, *J. Geophys. Res.*, 116(D8), D08203, doi:10.1029/2010JD014527, 2011.
- Slinn, W. G. .: Predictions for particle deposition to vegetative canopies, *Atmos. Environ.*, 16(7), 1785–1794,
605 doi:10.1016/0004-6981(82)90271-2, 1982.
- Su, L. and Fung, J. C. H.: Sensitivities of WRF-Chem to dust emission schemes and land surface properties in simulating dust cycles during springtime over East Asia, *J. Geophys. Res. Atmos.*, 120(21), 11,215-11,230, doi:10.1002/2015JD023446, 2015.
- Todd, M. C., Bou Karam, D., Cavazos, C., Bouet, C., Heinold, B., Baldasano, J. M., Cautenet, G., Koren, I., Perez, C., Solmon, F., Tegen, I., Tulet, P., Washington, R. and Zakey, A.: Quantifying uncertainty in estimates of mineral dust flux: An
610 intercomparison of model performance over the Bod éDépression, northern Chad, *J. Geophys. Res.*, 113(D24), D24107, doi:10.1029/2008JD010476, 2008.
- Uno, I., Wang, Z., Chiba, M., Chun, Y. S., Gong, S. L., Hara, Y., Jung, E., Lee, S.-S., Liu, M., Mikami, M., Music, S., Nickovic, S., Satake, S., Shao, Y., Song, Z., Sugimoto, N., Tanaka, T. and Westphal, D. L.: Dust model intercomparison (DMIP) study over Asia: Overview, *J. Geophys. Res.*, 111(D12), D12213, doi:10.1029/2005JD006575, 2006.
- 615 Wesely, M. L.: Parameterization of surface resistances to gaseous dry deposition in regional-scale numerical models, *Atmos. Environ.*, 23(6), 1293–1304, doi:10.1016/0004-6981(89)90153-4, 1989.
- Wu, C.-L. and Lin, Z.-H.: Uncertainty in Dust Budget over East Asia Simulated by WRF/Chem with Six Different Dust Emission Schemes, *Atmos. Ocean. Sci. Lett.*, 6(6), 428–433, doi:10.1080/16742834.2013.11447120, 2013.
- Wu, C.-L. and Lin, Z.-H.: Impact of two different dust emission schemes on the simulation of a severe dust storm in East Asia
620 using the WRF/Chem model, *Clim. Environ. Res. (in Chinese)*, 19(4), 419–436, doi:10.3878/j.issn.1006-9585.2013.13041, 2014.
- Wu, M., Liu, X., Zhang, L., Wu, C., Lu, Z., Ma, P. L., Wang, H., Tilmes, S., Mahowald, N., Matsui, H. and Easter, R. C.: Impacts of Aerosol Dry Deposition on Black Carbon Spatial Distributions and Radiative Effects in the Community Atmosphere Model CAM5, *J. Adv. Model. Earth Syst.*, 10(5), 1150–1171, doi:10.1029/2017MS001219, 2018.
- 625 Yuan, T., Chen, S., Huang, J., Zhang, X., Luo, Y., Ma, X. and Zhang, G.: Sensitivity of simulating a dust storm over Central Asia to different dust schemes using the WRF-Chem model, *Atmos. Environ.*, 207(March), 16–29, doi:10.1016/j.atmosenv.2019.03.014, 2019.
- Zaveri, R. A. and Peters, L. K.: A new lumped structure photochemical mechanism for large-scale applications, *J. Geophys. Res. Atmos.*, 104(D23), 30387–30415, doi:10.1029/1999JD900876, 1999.
- 630 Zaveri, R. A., Easter, R. C., Fast, J. D. and Peters, L. K.: Model for Simulating Aerosol Interactions and Chemistry (MOSAIC), *J. Geophys. Res. Atmos.*, 113(13), 1–29, doi:10.1029/2007JD008782, 2008.
- Zender, C. S., Miller, R. L. R. L. and Tegen, I.: Quantifying mineral dust mass budgets: Terminology, constraints, and current estimates, *Eos, Trans. Am. Geophys. Union*, 85(48), 509–512, doi:10.1029/2004EO480002, 2004.



- Zhang, J. and Shao, Y.: A new parameterization of particle dry deposition over rough surfaces, *Atmos. Chem. Phys.*, 14(22),
635 12429–12440, doi:10.5194/acp-14-12429-2014, 2014.
- Zhang, L. and He, Z.: Technical Note: An empirical algorithm estimating dry deposition velocity of fine, coarse and giant
particles, *Atmos. Chem. Phys.*, 14(7), 3729–3737, doi:10.5194/acp-14-3729-2014, 2014.
- Zhang, L., Gong, S., Padro, J. and Barrie, L.: A size-segregated particle dry deposition scheme for an atmospheric aerosol
module, *Atmos. Environ.*, 35(3), 549–560, doi:10.1016/S1352-2310(00)00326-5, 2001.
- 640 Zhang, L., Fang, G. C., Liu, C. K., Huang, Y. L., Huang, J. H. and Huang, C. S.: Dry deposition fluxes and deposition
velocities of seven trace metal species at five sites in central Taiwan - A summary of surrogate surface measurements and a
comparison with model estimations, *Atmos. Chem. Phys.*, 12(7), 3405–3417, doi:10.5194/acp-12-3405-2012, 2012.
- Zhang, X., Sharratt, B., Liu, L., Wang, Z., Pan, X., Lei, J., Wu, S., Huang, S.-Y., Guo, Y.-H., Li, J., Tang, X., Yang, T., Tian,
Y., Chen, X.-S., Hao, J.-Q., Zheng, H.-T., Yang, Y.-Y. and Lyu, Y.-L.: East Asian dust storm in May 2017: observations,
645 modelling, and its influence on the Asia-Pacific region, *Atmos. Chem. Phys.*, 18(11), 8353–8371,
doi:10.5194/acp-18-8353-2018, 2018.
- Zhang, X. X., Sharratt, B., Lei, J. Q., Wu, C. L., Zhang, J., Zhao, C., Wang, Z. F., Wu, S. X., Li, S. Y., Liu, L. Y., Huang, S. Y.,
Guo, Y. H., Mao, R., Li, J., Tang, X. and Hao, J. Q.: Parameterization schemes on dust deposition in northwest China: Model
validation and implications for the global dust cycle, *Atmos. Environ.*, 209(April), 1–13, doi:10.1016/j.atmosenv.2019.04.017,
650 2019.
- Zhang, Y., Zhang, X., Wang, L., Zhang, Q., Duan, F. and He, K.: Application of WRF/Chem over East Asia: Part I. Model
evaluation and intercomparison with MM5/CMAQ, *Atmos. Environ.*, 124, 285–300, doi:10.1016/j.atmosenv.2015.07.022,
2016.
- Zhao, C., Liu, X., Leung, L. R., Johnson, B., McFarlane, S. A., Gustafson, W. I., Fast, J. D. and Easter, R.: The spatial
655 distribution of mineral dust and its shortwave radiative forcing over North Africa: Modeling sensitivities to dust emissions and
aerosol size treatments, *Atmos. Chem. Phys.*, 10(18), 8821–8838, doi:10.5194/acp-10-8821-2010, 2010.
- Zhao, C., Liu, X., Leung, L. R. and Hagos, S.: Radiative impact of mineral dust on monsoon precipitation variability over West
Africa, *Atmos. Chem. Phys.*, 11(5), 1879–1893, doi:10.5194/acp-11-1879-2011, 2011.
- Zhao, C., Liu, X. and Leung, L. R.: Impact of the Desert dust on the summer monsoon system over Southwestern North
660 America, *Atmos. Chem. Phys.*, 12(8), 3717–3731, doi:10.5194/acp-12-3717-2012, 2012.
- Zhao, C., Chen, S., Leung, L. R., Qian, Y., Kok, J. F., Zaveri, R. A. and Huang, J.: Uncertainty in modeling dust mass balance
and radiative forcing from size parameterization, *Atmos. Chem. Phys.*, 13(21), 10733–10753, doi:10.5194/acp-13-10733-2013,
2013.
- Zhao, T. L., Gong, S. L., Zhang, X. Y., Abdel-Mawgoud, A. and Shao, Y. P.: An assessment of dust emission schemes in
665 modeling east Asian dust storms, *J. Geophys. Res. Atmos.*, 111(5), 1–11, doi:10.1029/2004JD005746, 2006.



Table 1. WRF-Chem configuration

Atmospheric Process	WRF-Chem option	Namelist Variable	Option
Surface Layer physics	Noah land-surface model	sf_surface_physics	2
Boundary Layer Physics	YSU scheme	bl_pbl_physics	1
Longwave/Shortwave Radiation	RRTMG	ra_lw(sw)_physics	4
Cumulus Clouds	Grell-Freitas	cu_physics	3
Cloud microphysics	Morrison double-moment	mp_physics	10
Gas-phase/aerosol chemistry	CBMZ/ MOSAIC 4-bin	chem_opt	9

670

675

680



685 **Table 2.** Three dry deposition schemes

Scheme	BS95	PE92	Z01
V_d	$V_d = V_g + \frac{1}{R_a + R_s + R_a R_s V_g}$	$V_d = V_g + \frac{1}{R_a + R_s}$	$V_d = V_g + \frac{1}{R_a + R_s + R_a R_s V_g}$
R_s	$R_s = \frac{1}{u_*(E_B + E_{IM})}$	$R_s = \frac{1}{u_*(E_B + E_{IM} + E_{IN})R}$	$R_s = \frac{1}{\epsilon_0 u_*(E_B + E_{IM} + E_{IN})R}$
E_{IM}	$E_{IM} = 10^{-st}$	$E_{IM} = \left(\frac{St}{0.8 + St}\right)^2$	$E_{IM} = \left(\frac{St}{\alpha + St}\right)^\beta$
E_{IN}	0	$E_{IN} = \frac{(0.0016 + 0.0061z_0)d_p}{1.414 \times 10^{-7}}$	$E_{IN} = \frac{1}{2} \left(\frac{d_p}{A}\right)^2$
R	1.0	$R_1 = e^{-2\sqrt{St}}$	$e^{-1.0\sqrt{St}}$
St	$St = \frac{u_*^2 v_g}{g v}$	$St = \frac{\rho_p d_p^2}{9 \mu d_c} u$	$St = \frac{v_g u_*}{g A} \text{(vegetated surfaces)}$ $St = \frac{v_g u_*^2}{g v} \text{(smooth surfaces)}$

690

695



Table 3. Model experiments and the corresponding model configuration in WRF-Chem. Note that the dust_opt =15 option for Shao2011 is added to WRF-Chem by ourselves.

700

Experiment name	Dust emission scheme	Dry deposition scheme	dust_opt	dust_schme	aer_drydep_opt
GOBS95	GOCART	BS95	13	/	1
GOPE92	GOCART	PE92	13	/	101
GOZ01	GOCART	Z01	13	/	301
S11BS95	Shao2011	BS95	15	3	1
S11PE92	Shao2011	PE92	15	3	101
S11Z01	Shao2011	PE92	15	3	301

705

710



715 **Table 4.** Correlation coefficient (R) and root mean square error (RMSE) between the model and observations for PM₁₀ over five sub regions and over whole China in Fig. 6 for six experiments listed in Table 3.

Region	R/RMSE	GOBS95	GOPE92	GOZ01	S11BS95	S11PE92	S11Z01
TD	R	0.64	0.53	0.59	0.34	0.37	0.37
TD	RMSE	79.61	91.91	106.61	124.25	119.54	115.68
GD	R	0.75	0.78	0.82	0.76	0.75	0.74
GD	RMSE	174.81	137.14	77.81	193.23	128.21	82.58
NCP	R	0.75	0.73	0.73	0.78	0.76	0.77
NCP	RMSE	231.2	221.05	197.43	189.08	164.25	107.20
NEP	R	0.62	0.63	0.58	0.70	0.68	0.68
NEP	RMSE	177.17	174.52	171.96	159.47	144.77	126.91
YR	R	0.45	0.42	0.43	0.67	0.61	0.61
YR	RMSE	105.96	105.97	93.97	94.07	93.79	69.94
Total	R	0.50	0.60	0.63	0.85	0.83	0.83
Total	RMSE	146.58	137.96	120.57	133.71	113.88	82.98



725 **Table 5.** Correlation coefficient (R) and root mean square error (RMSE) between the model and MODIS observation for
AOD for six experiments over the 7-day simulation period 1-7 May, 2017.

	GOBS95	GOPE92	GOZ01	S11BS95	S11PE92	S11Z01
R	0.32	0.37	0.27	0.40	0.39	0.42
RMSE	0.46	0.46	0.46	0.46	0.47	0.47

730

735

740



745 **Table B1.** Differences in Shao2011 dust emission scheme between different WRF-Chem versions

	Before WRF-Chem v3.8	WRF-Chem v3.8 and later
c_0	0.5	2.3
β	90	200
η_{mi}	/	/

750

755

760



Table B2. Percentage of each soil type in the whole East Asia domain

765

Soil type	Sand	Loamy sand	Sandy loam	Silt loam	silt	loam
percentage	2.6%	0.2%	4.0%	9.3%	0	47.6%
Soil type	Sandy clay loam	Silty clay loam	Clay loam	Sandy clay	Silty clay	clay
percentage	8.6%	0	21.7%	0	0.05%	6.0%

770

775

780

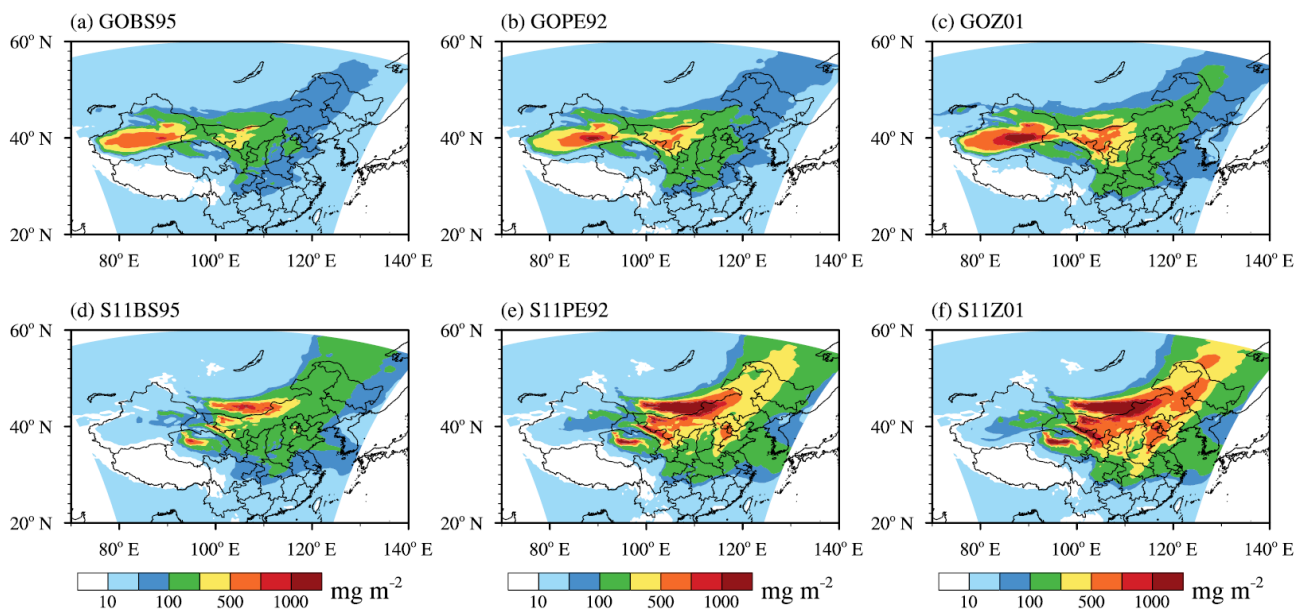


Table B3. Sensitivity of the simulated total dust emission from the Shao2011 to model parameters over the 7-day simulation period 1-7 May, 2017. The multiple of the dust emission of different cases is calculated with respect to the control run.

	C_0	β	η_{mi}	Dust emission (Tg)	Multiple
control run	2.3	200	12 types	1.35	1.00
case1	2.3	90	12 types	1.83	1.35
case2	0.5	200	12 types	0.29	0.21
case3	2.3	200	4 types	17.5	13.00

790

795



800

Figure 1. Spatial distribution of simulated mean dust loading for six experiments (a)GOBS95, (b)GOPE92, (c)GOZ01, (d)S11BS95, (e)S11PE92, (f)S11Z01 over the 7-day simulation period from 00:00 UTC on 1 May to 23:00 UTC on 7 May, 2017 (unit: mg m^{-2}).

805

810

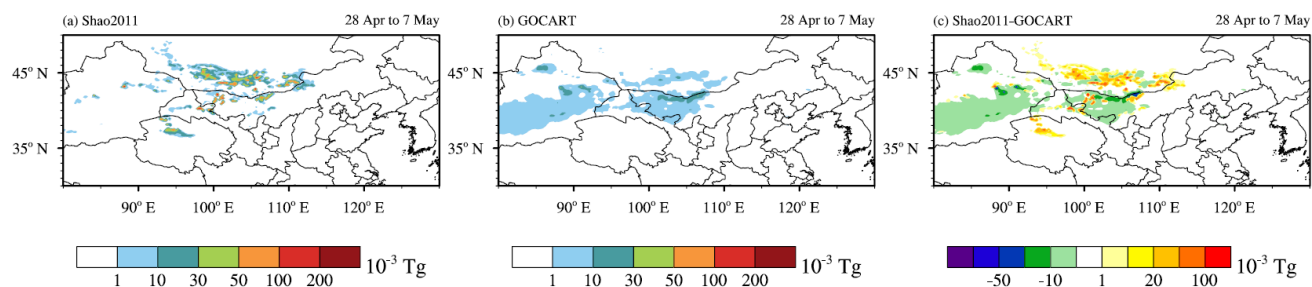
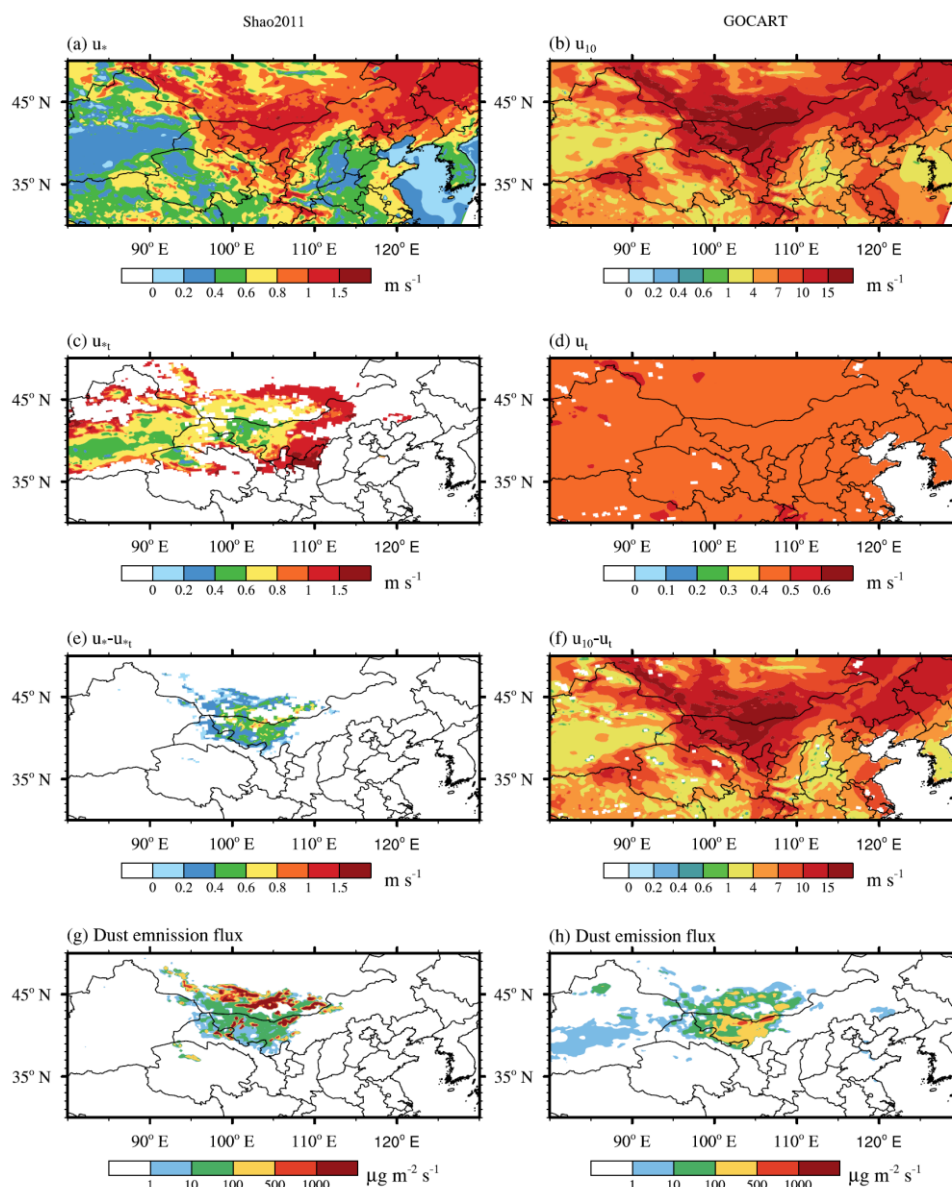


Figure 2. The simulated total dust emission (10^{-3} Tg) from two dust emission schemes: (a) Shao2011 and (b) GOCART from 00:00 UTC on 28 April to 23:00 UTC on 7 May, 2017. (c) The total dust emission flux difference between Shao2011 and GOCART. The diameter of the emitted dust is less than $10\ \mu\text{m}$ in both GOCART and Shao2011 dust emission schemes.

815



820

Figure 3. Spatial distribution of (a) friction velocity (u_*), (c) threshold friction velocity (u_{*t}) and (e) the difference between u_* and u_{*t} ($u_* - u_{*t}$) from Shao2011 dust emission scheme at 06:00 UTC on 3 May, 2017; (b) wind speed at 10 meters (u_{10}), (d) threshold velocity (u_t) and the difference between u_{10} and u_t ($u_{10} - u_t$) from GOCART dust emission scheme at 06:00 UTC on 3 May, 2017. Spatial distribution of (g) dust emission flux from Shao2011, (h) dust emission flux from

825 GOCART at 06:00 UTC on 3 May, 2017.

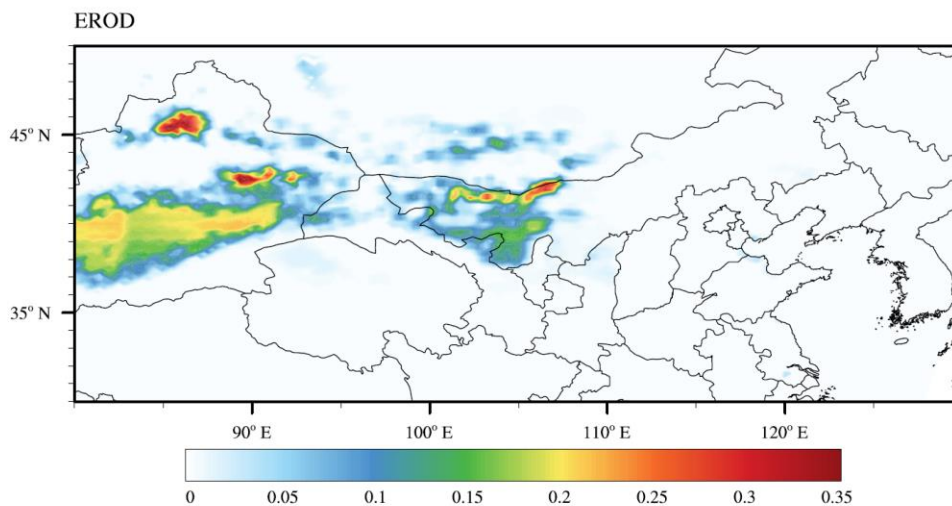


Figure 4. The fraction of erodible surface in each grid cell used in GOCART dust emission scheme.

830

835

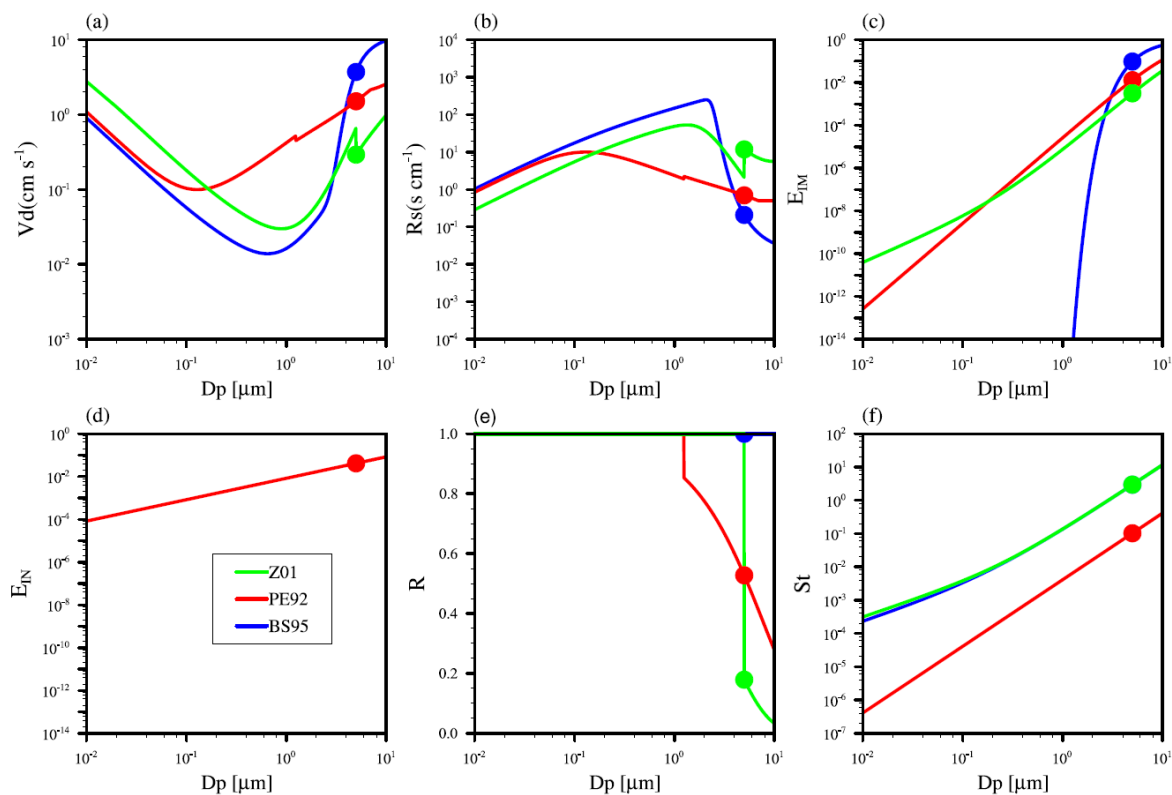
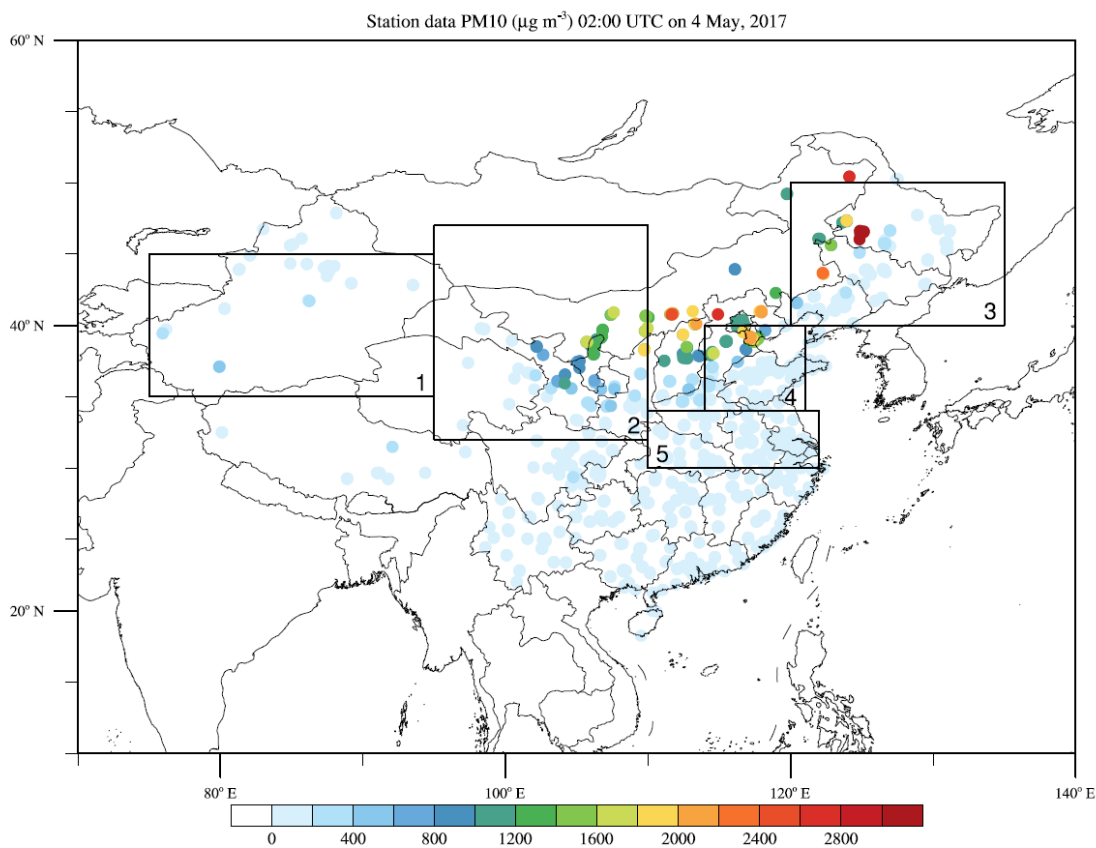
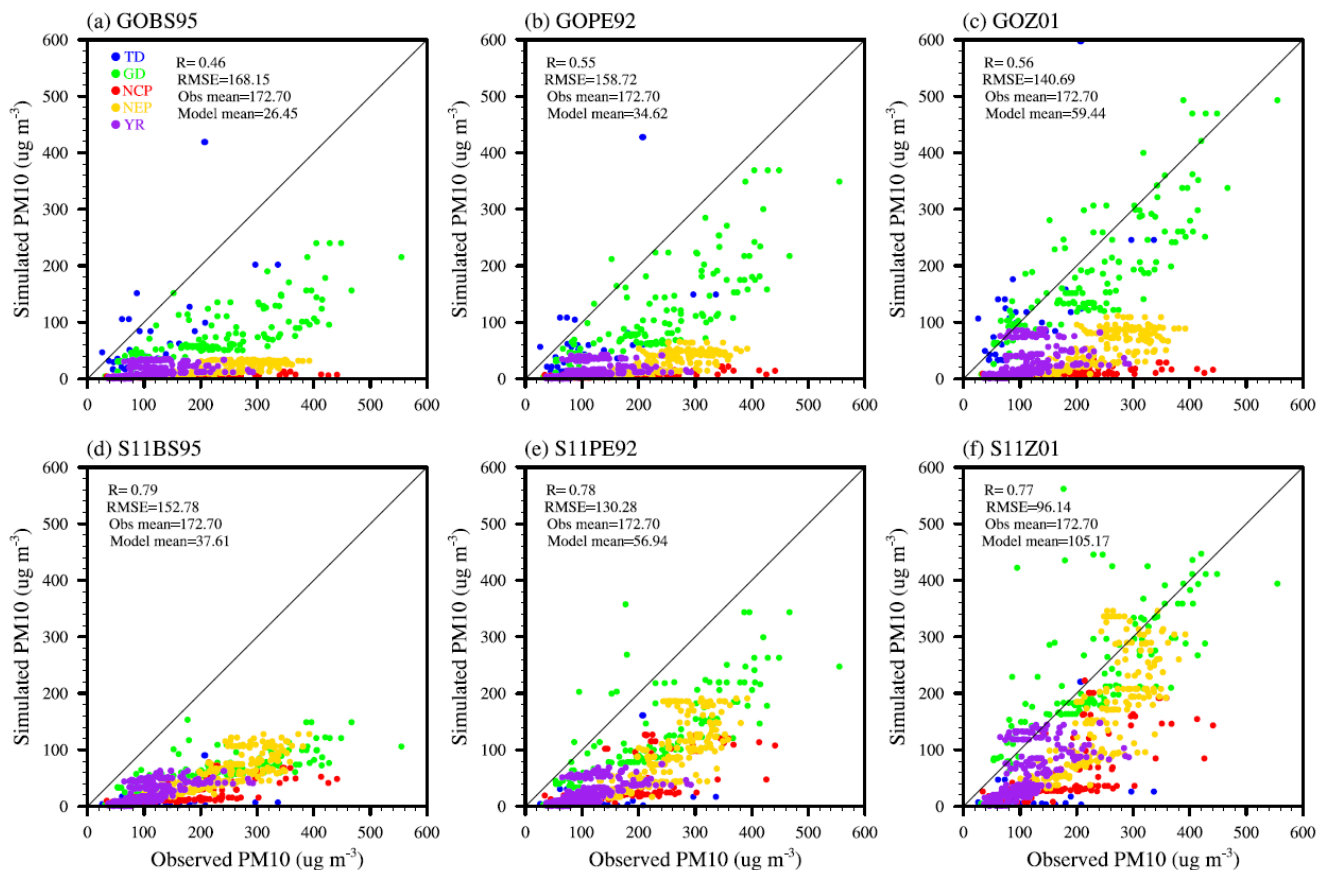


Figure 5. (a) Dry deposition velocity (V_d), (b) surface resistance (R_s), (c) surface collection efficiency from impaction (E_{IM}), (d) surface collection efficiency from interception (E_{IN}), (e) rebound (R) and (f) stokes number (St) as a function of particle diameter (D_p) over desert surface computed using different dry deposition schemes (BS95, PE92 and Z01). The colored dots

840 indicate at the reference diameter of $5 \mu\text{m}$.



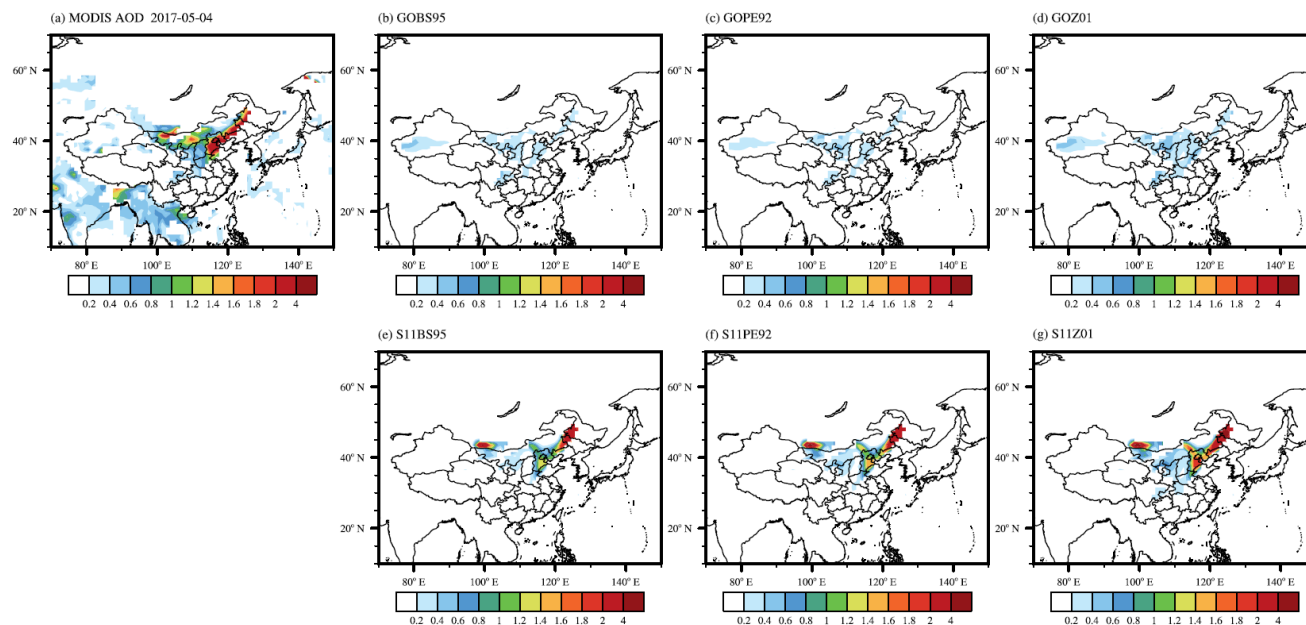
845 **Figure 6.** Five sub regions and observed PM₁₀ concentrations. “1” represents Taklimakan Desert (TD), “2” represents Gobi Desert (GD), “3” represents Northeastern plain (NEP), “4” represents North China Plain (NCP), “5” represents Middle and lower reaches of Yangtze River Plain (YR). The colored dots represent observed PM₁₀ concentrations over observational sites at 02:00 UTC on 4 May, 2017 (10:00 Beijing Time (BJT) on 4 May, 2017).



850

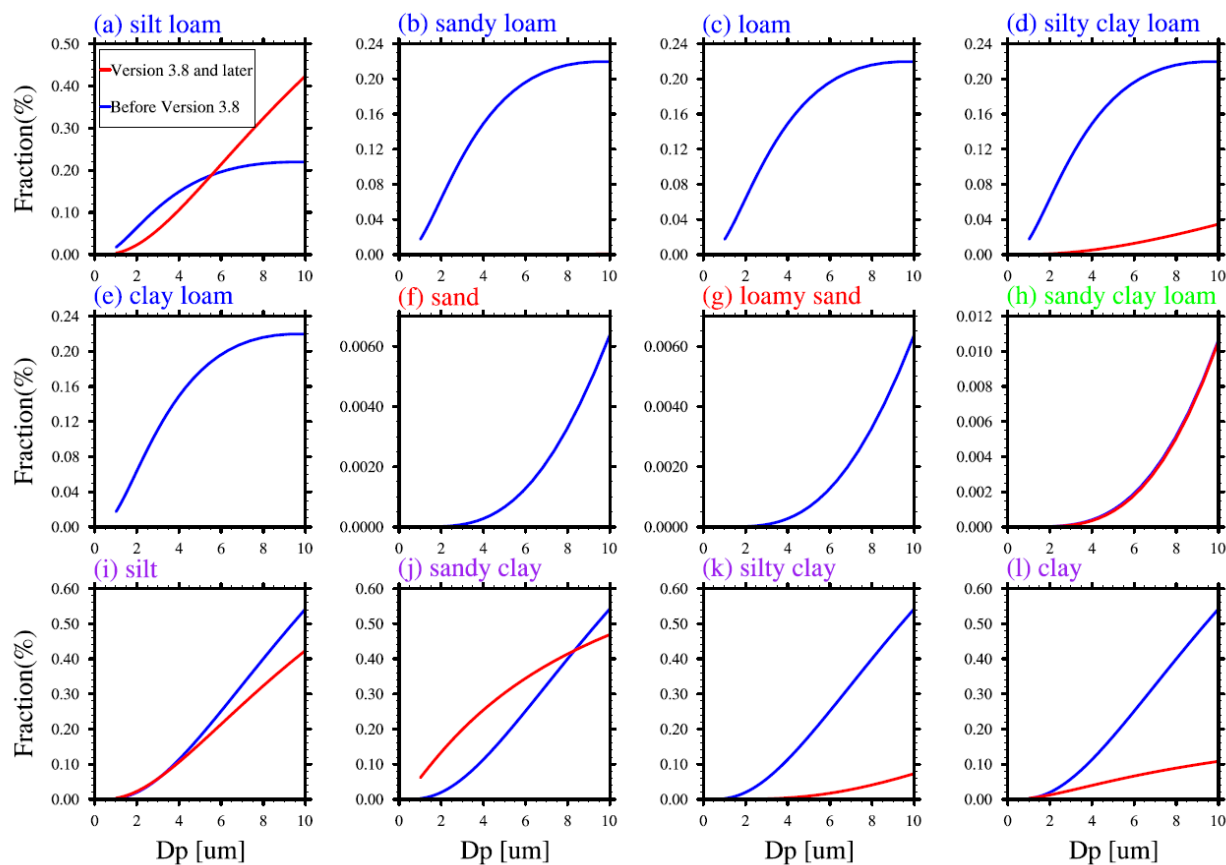
Figure 7. Simulated PM₁₀ versus observed PM₁₀ for six experiments (a)GOBS95, (b)GOPE92, (c)GOZ01, (d)S11BS95, (e)S11PE92, (f)S11Z01 over the 7-day simulation period 1-7 May, 2017. “Obs mean” is mean PM₁₀ from observation, “Model mean” is mean PM₁₀ from simulation, “R” is the correlation coefficient between model and observations, “RMSE” is the root mean square error. Different color dots represent different regions as shown in Fig. 6.

855



860

Figure 8. Simulated and observed AOD on 4 May, 2017: (a) Distribution of daily mean aerosol optical depth (AOD) at 550 nm derived from MODIS-Aqua; WRF-Chem simulated AOD at 13:00 p.m. local time for six experiments (b) GOBS95, (c) GOPE92, (d)GOZ01, (e)S11BS95, (f)S11PE92, (g) S11Z01. The simulated AOD already collocated with MODIS AOD.



865

Figure B1. Free dust fraction for 12 soil types as a function of particle diameter (D_p). The red lines represent the free dust fraction in WRF-Chem v3.8 and later versions. The blue lines represent the free dust fraction before WRF-Chem v3.8. The colors of the soil type font in the upper left corner of the plot are different. In WRF-Chem v3.8 and later versions, each soil type has a corresponding free dust fraction distribution. In versions before WRF-Chem v3.8, several soil types share a free dust fraction distribution. The same soil type font color indicates that a free dust fraction is shared among these soil types in versions before WRF-Chem v3.8.

870